Geofísica Internacional (2005), Vol. 44, 4, pp. 317-330

Source process and stress change associated with the 11 January, 1997 (Mw=7.1) Michoacán, Mexico, inslab earthquake

Miguel A. Santoyo, Shri K. Singh and Takeshi Mikumo
Instituto de Geofísica, UNAM, México, D.F., México

Received: January 20, 2005; accepted: March 17, 2005

RESUMEN

Con base en registros sísmicos obtenidos a distancias locales, regionales y telesísmicas, estudiamos las características de la fuente y el cambio de esfuerzos asociado del sismo de Michoacán del 11 de enero de 1997. Este evento fue localizado justo bajo la zona de ruptura del gran sismo de subducción de Michoacán de 1985. De la inversión de datos telesísmicos, obtenemos una falla cercana a la vertical a 35 km de profundidad, con una duración total de la fuente de 15 segundos, una magnitud de momento sísmico Mw=7.1 y una velocidad de ruptura promedio de 2.8 km/seg. El análisis de registros locales y telesísmicos muestra que la ruptura presentó una fuerte directividad al sureste, con una función de tiempo de la fuente compleja, dos subeventos principales y una duración de 13 segundos. La distribución de dislocaciones sobre el plano de falla, obtenida a partir de inversión lineal cinemática 2-D y con datos locales y telesísmicos de banda ancha, muestra un patrón de ruptura complejo donde la mayor parte de la liberación de momento sísmico ocurre en la porción sureste de la falla. La comparación entre los cambios de esfuerzos de Coulomb cosísmicos debido al evento principal, y la localización y el mecanismo focal de sus réplicas, sugiere que la sismicidad post-sísmica pudo haber sido disparada por los cambios de esfuerzos debidos al sismo principal.

PALABRAS CLAVE: Inversión cinemática de la fuente, esfuerzos de Coulomb, interacción de sismos.

ABSTRACT

We study the source characteristics and the associated coseismic stress change of the January 11, 1997 Michoacán earthquake, based on teleseismic, regional and near-source recordings. This event was located just beneath the ruptured zone of the 1985 Michoacán thrust event. From the inversion of teleseismic recordings, we obtain a nearly-vertical faulting at 35 km depth, a total source duration of 15 sec, a moment magnitude of Mw=7.1, and a mean rupture velocity of 2.8 km/sec. An analysis of teleseismic and local seismograms shows that the rupture had a strong directivity to the southeast, with a rather complex source-time function with two main subevents and a total duration of 13 sec. The dislocation distribution obtained from 2D kinematic linear inversion, using both local strong motion and broad-band teleseismic data, shows a complex rupture pattern with the main seismic moment release occurring in the southwest portion of the fault. A comparison between the coseismic Coulomb failure stress change during the main shock, and the location and mechanism of the aftershocks, suggests that post-event seismicity may have been triggered by the stress changes due to the main event.

KEY WORDS: Kinematic source inversion, Coulomb failure stress, earthquake interaction.

INTRODUCTION

The 11 January, 1997 earthquake (Mw=7.1) took place just beneath the area of the main ruptured zone of the great 1985 Michoacán earthquake (Mw=8.1), within the subducted slab, after a relatively short period of 12 years (Figure 1). The focal mechanism and other source parameters preliminarily reported by different institutions and authors (see Table 1) showed an intermediate-depth, nearly-vertical faulting event. From teleseismic waveform inversion, M. Kikuchi (personal communication, 1997) obtained a general dislocation pattern with two main asperities to the southeast side of the rupture area, under the assumption that the vertical nodal plane was the fault plane. Mikumo *et al*. (2000) calculated the dynamic stress change inside the fault area of this earthquake, based on the slip distribution obtained only from the local seismograms. They found that high stress drop zones are confined to the deeper part of the fault, surrounded by zones with low stress drop.

In this study, by the aid of teleseismic, regional and local recordings, we investigate in detail the main source characteristics (location, depth, focal mechanism, fault-plane orientation, directivity and complexity of the rupture), the distribution of dislocations, and the associated stress change in a 3D space and its relation with the aftershock seismicity.

FOCAL CHARACTERISTICS USING TELESEISMIC DATA

In order to retrieve a more reliable focal solution than those obtained by automated procedures, we inverted the

teleseismic body-wave recordings for point- and line-sources, using the Nábêlek's (1984) maximum-likelihood inversion technique. For this purpose, we low-pass filtered the available long period P and SH velocity waveform data using a Butterworth filter (F_c=0.5 Hz), selecting waveforms with a good signal to noise ratio.

The selection process yielded recordings from 23 teleseismic stations located at distances between 30°-92°, with a good azimuthal coverage (see Figure 2). The recordings were also corrected for the instrumental response, rotated, and integrated once in order to obtain the transverse and radial displacement time histories.

The crustal velocity model in the source region is based on the one obtained by Fuentes (1997), and adjusted by a grid search analysis of the P and S wave arrival times from the 16/1/97 aftershock local recordings. The 16/1/97 aftershock was considered as an empirical Green function of the mainshock event, due to its magnitude (Mw=5.5) and its hypocentral location, which occurred close enough to the mainshock hypocenter to consider that the body waves from the two events sample the same structure in the source region. In Table 2 we show the crustal model that provides the best fit to the arrival times to the local stations that recorded this aftershock. For the teleseismic receivers, we used the global crustal velocity model shown in Table 3. Here we also

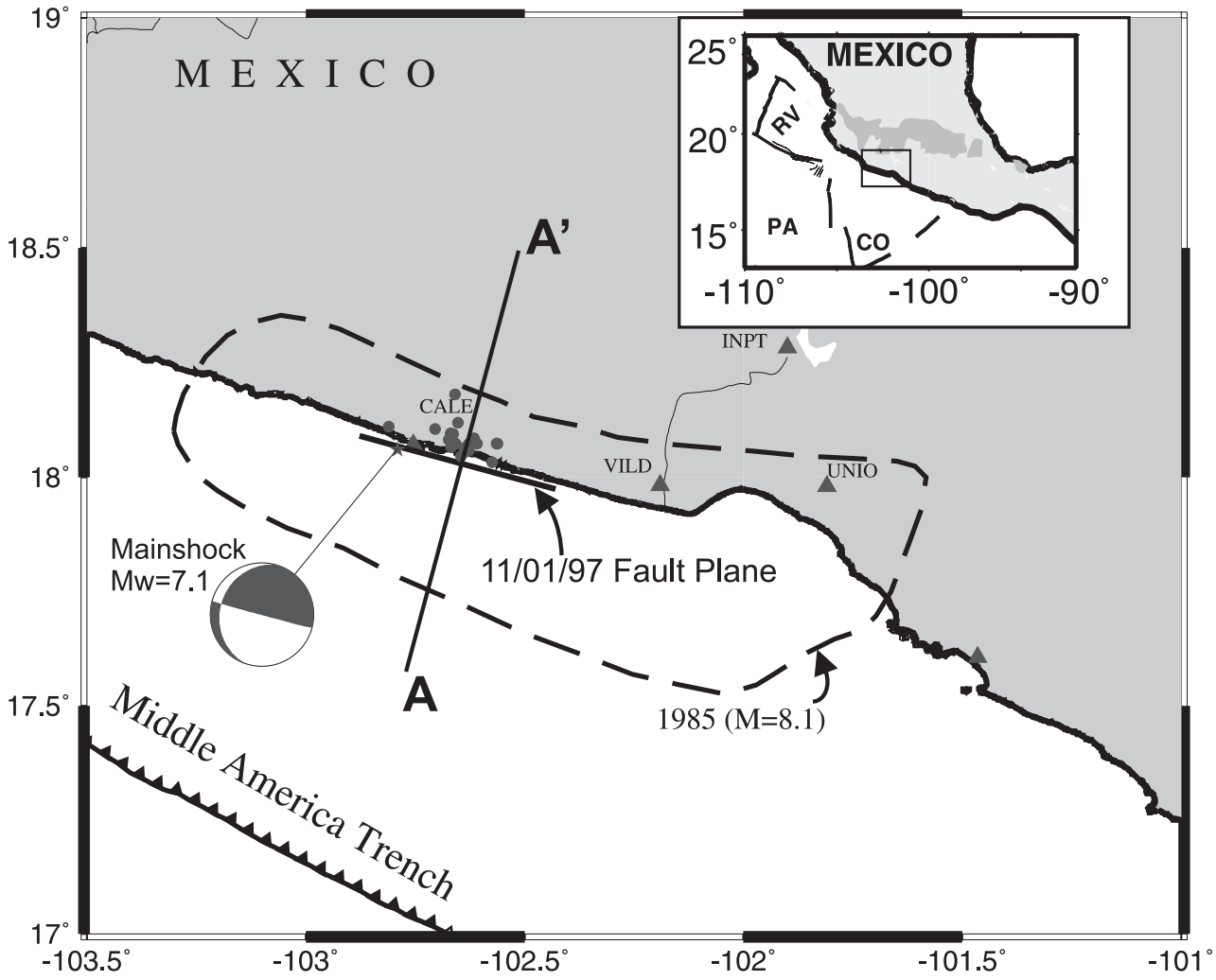

Fig. 1. Map of the epicentral region of the 11/01/1997 earthquake. Local strong motion stations are indicated by solid triangles. CALE= Caleta de Campos; VILD= La Villita; INPT= Infiernillo; UNIO= La Unión. The mainshock epicenter is shown by a solid star. Aftershocks are shown by solid dots. The projection of the fault plane on the surface is shown as a solid line almost parallel to the coast. Aftershocks area of the 1985 Michoacán earthquake is shown with a closed dotted line (UNAM Seismology Group, 1986). Line A-A' indicate the location of the cross section plane for stress computations (see text). *Inset:* Tectonic setting for the south Pacific coast of Mexico. PA= Pacific plate; CO= Cocos plate; RV=Rivera plate; continental Mexico belongs to the North America plate. The location of the epicentral region is indicated by a rectangle.

Table 1

Source parameters of the mainshock of 11 January 1997

Time (H: M: S)	Latitude (°N)	Longitude (°W)	Depth (km)	Mo. (Dyn-cm)	Focal Mech. (Str, Dip, Rake)	Duration (Sec)	Source
20:28:39.6	18.34	102.58	40	6.06×10^{26}	292, 82, -106	18.8	1
20:28:25.7	18.25	102.81	13	5.5×10^{26}	115, 90, 93	---	2
20:28:25.0	18.72	102.57	31	4.82×10^{26}	289, 81, -96	---	3
---	18.25	102.81	40-50	5.2×10^{26}	119, 90, 97	17.0	4
20:28:25.7	18.25	102.80	13	1.12×10^{27}	278, 10, 73	30.0	5
20:28:29.0	18.06	102.79	35	4.51×10^{26}	105, 87, -110	14.0	6

Sources: 1. Harvard University CMT catalog. 2. NEIC, United States Geological Survey. 3. Earthquake Research Institute, Tokyo University. 4. M. Kikuchi, personal communication. 5. Source time function catalog, University of Michigan. 6. This work.

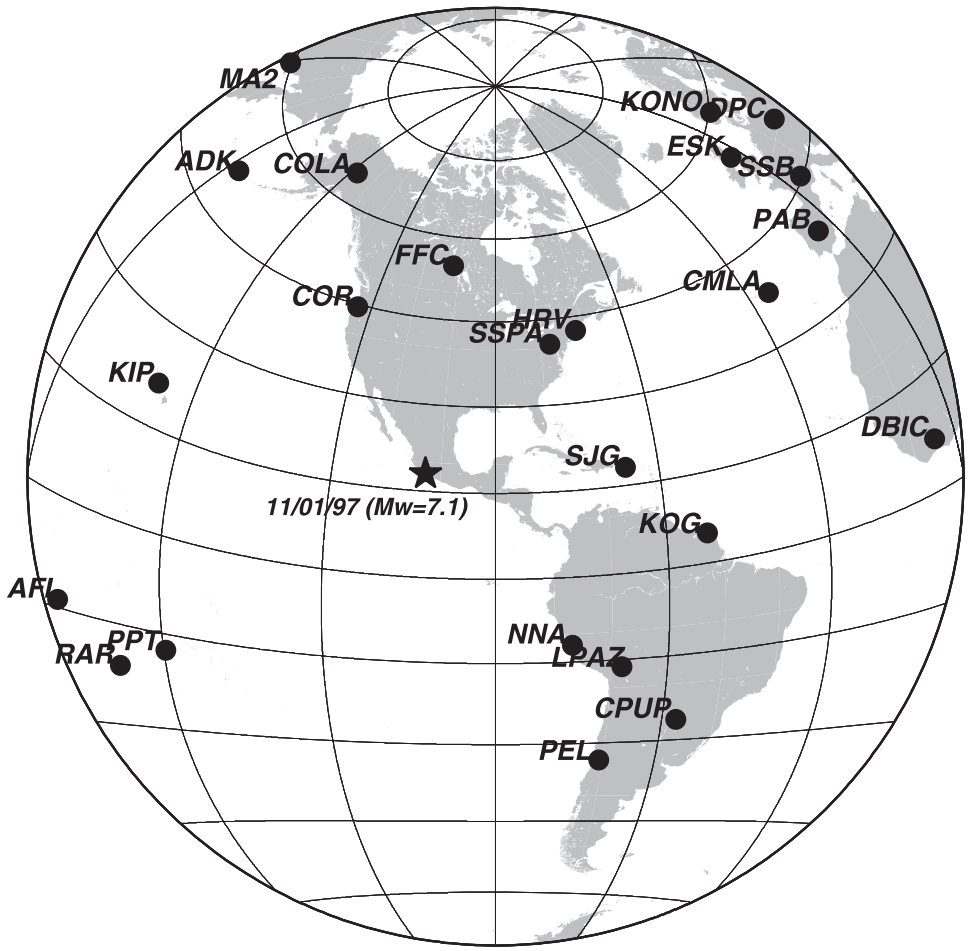

Fig. 2. World map showing, the teleseismic stations used in this study.

included the attenuation parameter T* (Futterman, 1962) of 1.0 second for P waves and 4.0 seconds for S waves. The epicenter location used here (18.06°N, 102.79°W) was relocated using local and regional seismograms.

Comparing the SH waveforms among some stations located in opposite directions from the epicenter (e.g. NNA and FFC; see Figure 3), we found a significant difference in their duration, which indicates a strong directivity effect. As

Table 2

Crustal velocity model for the source region

h‡ (km)	α* (km/sec)	β** (km/sec)	ρ# (gr/cm³)
0.0	5.3	3.35	2.50
4.0	6.0	3.45	2.76
15.0	6.5	3.80	2.84
35.0	7.4	4.27	2.90

Notes: ‡h= Depth of the upper interface; ∗α = P wave Velocity; ∗∗β= S wave velocity; #ρ= Density of the medium.

Table 3

Crustal velocity model for teleseismic receivers

h‡ (km)	α* (km/sec)	β* (km/sec)	ρ# (gr/cm³)
0.0	6.10	3.52	2.70
60.0	7.80	4.45	3.40

Notes: ‡h = Depth of the upper interface; ∗α = P wave Velocity; ∗∗β = S wave velocity; #ρ= Density of the medium.

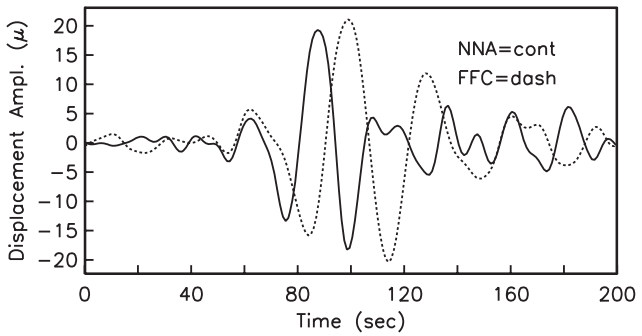

Fig. 3. S waveform displacements in the transverse component, obtained at NNA and FFC stations from the 11/01/97 mainshock. Note a shortened S wave pulse at station NNA (solid line) located southeast of the epicenter, and the broadened pulse at station FFC (dashed line) located northwest of the epicenter.

this effect was also observed at many other teleseismic and local stations, we performed a teleseismic directivity analysis. Here, we initially modeled the event as a propagating horizontal line source with velocity Vr, measuring the rms-errors with respect to the azimuth and the rupture velocity. In Figure 4a, we find that the minimum RMS for the directivity falls around the value of Az=105°, and the rupture velocity between Vr=2.6 km/sec and Vr=2.8 km/sec (Figure 4b). After these analyses, we performed the waveform inversion for the focal mechanism, depth and source time function. Results show an almost vertical dip-slip faulting mechanism, strike=105°, dip=89°, rake=110°, with a source time function duration of 15 sec and a centroid depth of 34 km. The RMS error in this case is E_{rms}=4.94x10^{-2} μ. Figures 5a and 5b show the resulting focal mechanism and the observed and synthetic seismograms of P and SH waves. Comparing this error with that obtained from the inversion using a single point source (E_{rms}=6.01x10^{-1} μ), we found a better agreement for the horizontally propagating source. This line source waveform inversion yielded an average seismic moment release of Mo=4.9x10^{26} dyn-cm (Mw=7.1).

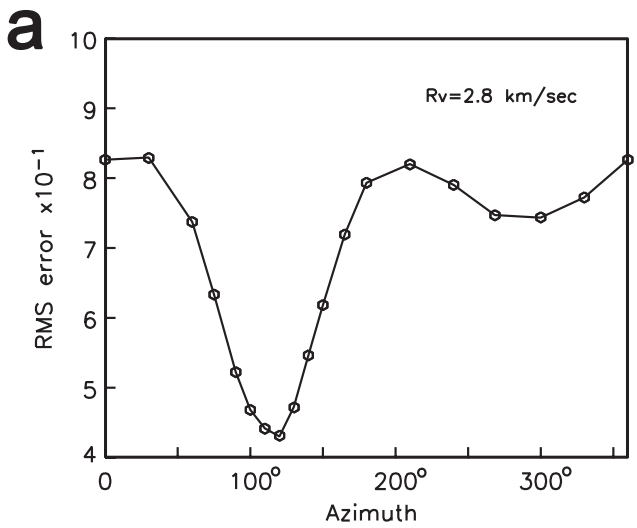

Fig. 4a. RMS errors for the teleseismic inversion vs directivity azimuth of a line source with horizontal rupture propagation. The lowest RMS corresponds to an azimuth of 105°.

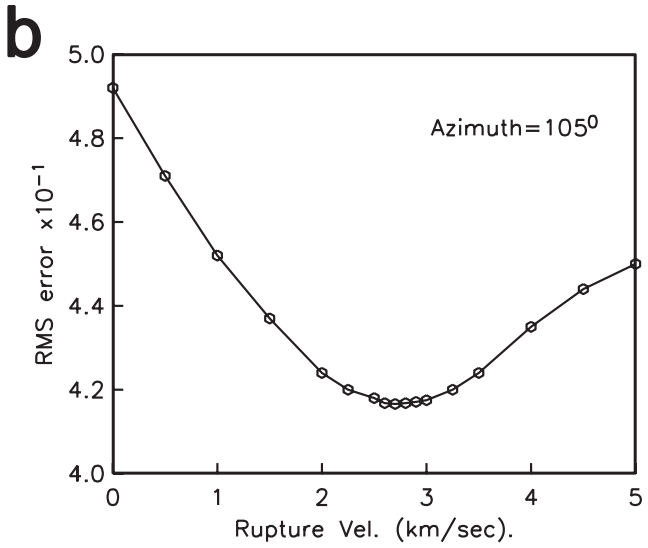

Fig. 4b. RMS errors for the teleseismic inversion vs rupture velocity for a line source with horizontal rupture propagation, with an azimuth of 105°. The lowest RMS errors occurr for values of Rv between 2.7 and 2.9 km/sec.

Table 4

Source parameters of the 11/01/97 aftershocks

Date (Y,M,D)	Lat (°N)	Lon (°W)	Depth (km)	M (Mw)	Focal Mech. (St; Dp; Rk)		
97-01-16	18.095	102.669	33	5.5	310	60	90
97-10-25	18.181	102.659	34	3.9	315	60	80
97-11-20	18.11	102.81	28	4.1	280	40	70
98-01-15	18.105	102.705	30	3.5	280	45	90
00-04-11	18.094	102.663	34	5.3	290	60	95
00-08-09-1	18.073	102.564	32	6.5	294	48	93
00-08-09-2	18.033	102.574	34	5.2	315	85	120
00-08-09-3	18.082	102.673	29	4	289	70	130
00-08-09-4	18.045	102.646	31	4.7	280	70	110
00-08-09-5	18.063	102.638	31	4.5	270	55	95
00-08-09-6	18.072	102.628	37	3.9			
00-08-10	18.073	102.562	39	4.5	280	65	120
00-08-12	18.066	102.668	32	3.5			
00-08-13-1	18.073	102.609	34	4.6	300	65	130
00-08-13-2	18.073	102.658	36	4.1	305	70	90
00-08-14	18.085	102.615	37	4.4	270	65	125
00-11-27	18.055	102.636	32				
00-08-18	18.119	102.652	31	3.6	310	70	80
00-12-01	18.058	102.628	31	5.5	285	70	120

Notes: All focal parameters were calculated from local strong motion data. Lat=Latitude; Lon=longitude; M= Magnitude; St= strike angle; Dp= Dip angle; Rk= Rake angle.

KINEMATIC ANALYSIS OF THE SOURCE

To investigate the slip distribution and the rupture history at the source, we performed a kinematic inversion using first only local strong-motion recordings, and second both local strong motion and broadband teleseismic data. Synthetic seismograms for local and regional distances were computed using the discrete wave-number method described by Bouchon and Aki (1977) and Bouchon (1979). For teleseismic distances the synthetics were computed using the generalized ray theory procedure proposed by Helmberger (1974), and Langston and Helmberger (1975). The crustal velocity structure around the source region used in both methods was the same as shown in Table 2.

Kinematic analysis using strong-motion seismic recordings

For this purpose, we selected the recordings from four closest, three-component accelerograph stations: CALE, VILD, INPT and UNIO (Figure 1). This choice is based on the fact that near-soure records are less contaminated by path propagation effects. In Figure 1 we also show the epicentral locations of the mainshock and its aftershocks (Table 4). The acceleration records were integrated once following the procedure proposed by Iwan *et al*. (1985) to obtain the ground velocities, and then low-pass filtered (Fc=1.0 Hz) using a three pole Butterworth filter. Recordings from stations CALE (EW), UNIO (NS and EW) and VILD (EW) are contaminated by some undesirable glitches, so we un-glitched the seismograms by averaging the adjacent acceleration values before the processing of the data.

We performed a 2D finite source inversion of the slips over the source plane, using only local and regional data. In order to discriminate the actual fault plane from the two nodal planes, we observed that the nearly-vertical plane meets important constraints: First, the vertical plane becomes nearly parallel to the coast and to the trench, which is not the case for the auxiliary plane. Second, as we will see later, kinematic inversion over the vertical fault plane gives a better fit between the synthetic and observed seismograms than for the auxiliary plane.

To obtain the slip distribution over the nearly-vertical fault plane, we discretized it into 416 square subfaults of equal size (2.0 km x 2.0 km), embedded in a horizontally layered structure. Based on this assumption, the observed data together with the synthetic seismograms computed us-

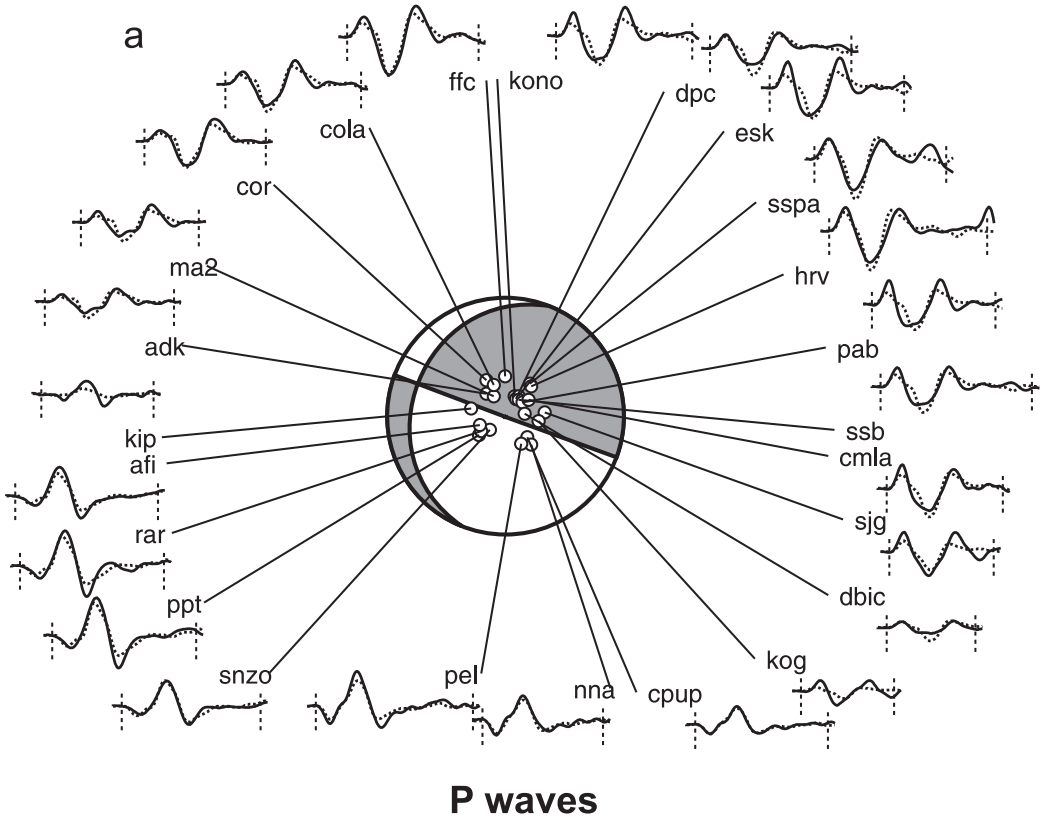

Fig. 5a. Focal mechanism and P waveforms fit for the 11/01/97 mainshock, obtained from the teleseismic inversion. Recorded waveforms are shown by solid lines, and synthetic seismograms are shown by dashed lines. Stations are shown located in the lower focal hemisphere with open circles.

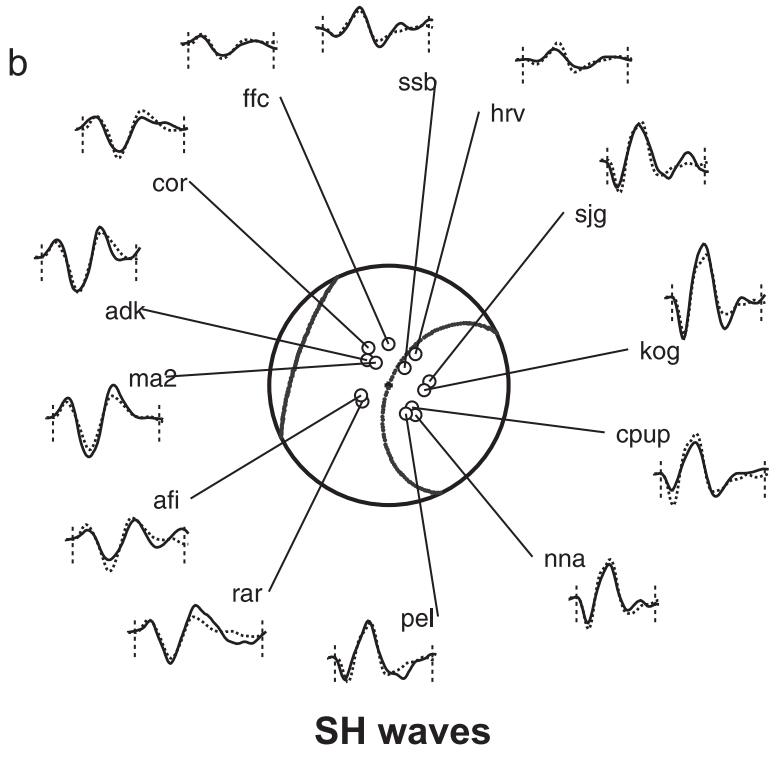

Fig. 5b. SH wave inversion results from the teleseismic inversion. Recorded waveforms are in solid lines, and synthetic seismograms are shown by dashed lines.

ing the techniques already mentioned, form an over-determined linear system of the type **AX≈B**. Here, the matrix **A** contains the synthetic seismograms with its respective time shifting due to the rupture, **B** is a vector with the observed records arranged in the same order as in the synthetics in matrix **A**, and **X** is the solution vector containing the dislocation weighting values which represent the amount of slip that must be applied to each subfault in order to fit the observations.

The matrix equation shown here can be solved by a simple least-squares technique; however, the solution becomes unstable because matrix **A** could be ill-conditioned (Hartzell and Heaton, 1983). To solve this problem, the inversion was stabilized by a Householder decomposition of the matrix equations (Lawson and Hanson, 1974; Menke 1984), and imposing a positivity constraint to the solution. To further stabilize the inversion, we appended to the linear system, additional smoothing and moment-minimization constraints of the form $\lambda\mathbf{FX}=\lambda\mathbf{D}$, where λ is a scalar weighting factor. Smoothing is imposed by constructing **F** and **D** such that the difference between adjacent dislocations is zero. Moment minimization is obtained by letting **F** be the identity matrix and **D** the zero vector, effectively reducing the length of **X**. To identify the proper weighting factor λ, several inversion runs are conducted until the largest value of λ is reached that still allows the observed records to be fitted by the synthetic waveforms. In this case, spatial smoothness constraints are imposed to reduce some noise effects included in the solution, which could come from some unconsidered path effects or the simplification of the velocity model.

For the kinematic inversion, we again assumed a constant rupture velocity of 2.8 km/sec (same as that estimated from the teleseismic analysis), as this produced a more coherent solution and better fit between the observed and synthetic seismograms. Due to this constant rupture velocity, the rupture initiates at the hypocenter and propagates with circular rupture fronts. We assumed also that the value of the rise time was the same for all the subfaults. Following this assumption, the rise time value was varied in different inversion runs, between 0.5 and 2.0 seconds to obtain a value that best fit the observations. In this case, we obtained a mean source duration of 1.2 seconds. As mentioned earlier, the fault plane was discretized into a uniform mesh of 2.0 km x 2.0 km, obtaining a total of 416 subfaults, using the focal mechanism obtained from the teleseismic inversion (strike=105°, dip=89°). The rupture initiation point was located at 10 km from the northwestern edge, and 14 km from the upper edge of the fault.

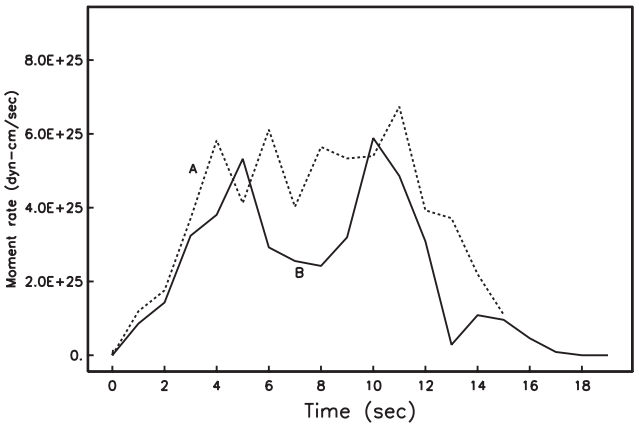

Fig. 6. Source time functions for the 11/01/97 mainshock, obtained in this study from three different inversions. Curves A and B indicate source time functions obtained from 2-D dislocation linear inversion, and joint inversion of local and teleseismic seismograms, respectively. The amplitudes are in dyn-cm/sec.

The inversion results show a good agreement between the synthetic and observed velocity seismograms with an RMS error of $1.53\text{x}10^{-2}$ cm/sec (Figure 7a). It can be observed that the rupture propagates almost horizontally from the hypocenter to the southeast direction. The dislocation pattern obtained (Figure 7b) is mainly confined to depths between 25 km and 50 km with a horizontal length of approximately 35 km. It can also be observed that the main asperity with the largest moment release is located at the southeastern side of the fault plane close to the end of the rupture, 20 to 30 km southeast of the hypocenter. The maximum slip here obtained from this inversion is 450 cm and the total seismic moment release is Mo= $4.6\text{x}10^{26}$ dyn-cm respectively. The total overall time duration obtained for the source time function (curve A, Figure 6) is about 13 seconds with two main subevents: the first one 4 seconds after the initiation of the rupture, and the second and largest one, approximately 11 seconds after the initiation time, during the last phase of the rupture. The dimension of the main ruptured asperity (second subevent) is about 15x20 km, as shown in the dislocation pattern in Figure 7b.

As a further check on the vertical plane as the real fault plane, we performed tests following a procedure by Delouis and Legrand (1999). Here, we inverted the waveforms at the same stations, but taking the auxiliary plane as the fault plane. In this case we used the same parameters as for the nearly-vertical plane. The RMS errors of the misfit between the observed and synthetic seismograms for the two planes are significantly different: $2.37\text{x}10^{-2}$ cm/sec for the auxiliary plane and $1.53\text{x}10^{-2}$ cm/sec for the vertical plane. On the other hand, the slip distribution obtained over the auxiliary plane was very dispersed, contrary to the pattern observed for the vertical plane. These results clearly show that the horizontal plane could hardly represent the real fault plane.

Joint inversion for slips over the fault plane using local and teleseismic data

A large number of broadband teleseismic stations between 30° and 95° recorded the mainshock event with a good

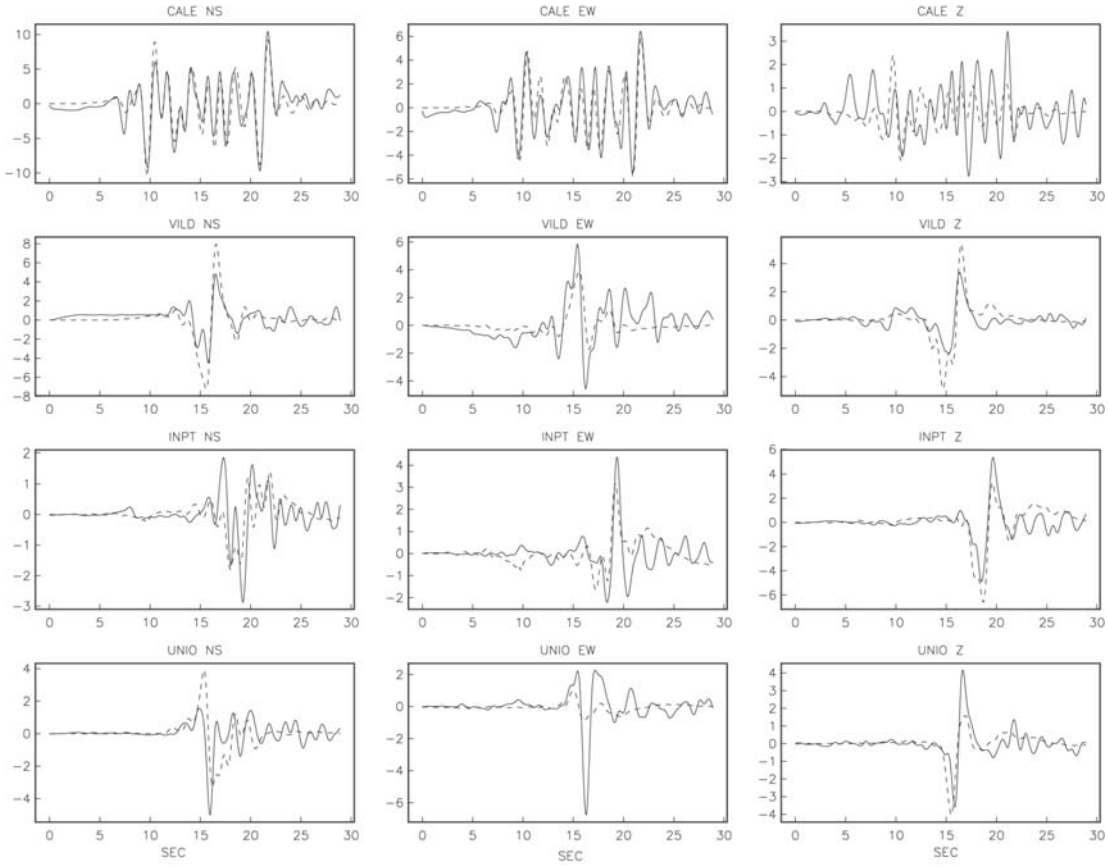

Fig. 7a. Comparison between the recorded (solid lines), and synthetic velocity seismograms (dashed lines) for the four local stations used in this study, for the 2-D kinematic inversion.

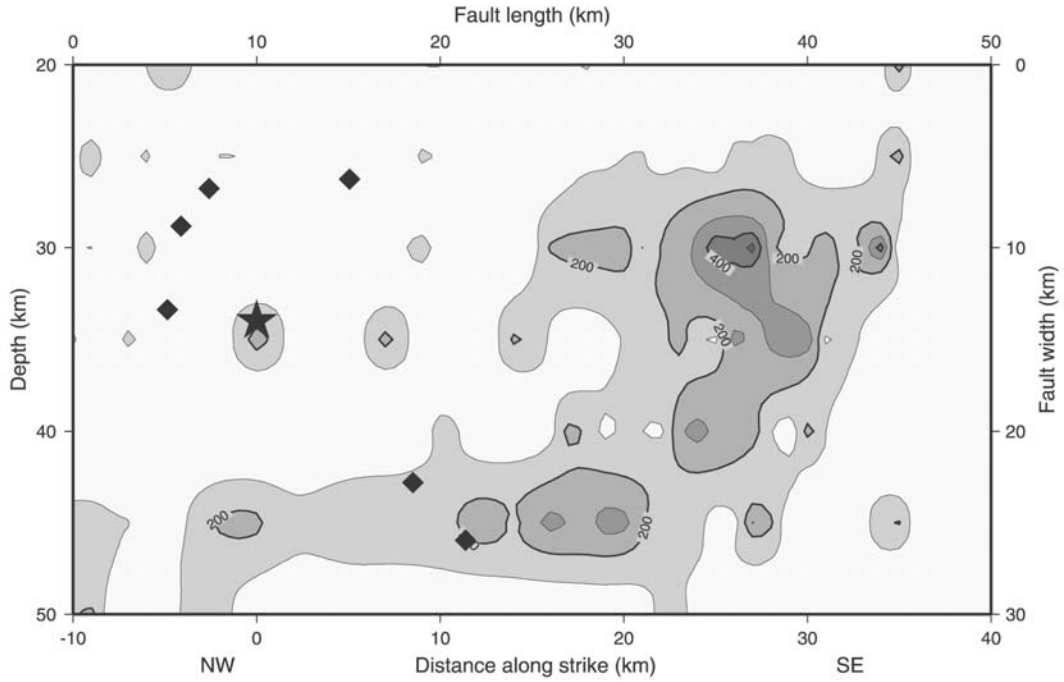

Fig. 7b. Dislocation pattern obtained from the 2-D kinematic inversion. Slips are shown in cm. The main rupture asperity is located at the S-E portion of the fault plane. Fault plane is viewed from southwest. Depths are given in km. The upper edge of the fault plane is located at a depth of 20 km.

azimuthal coverage. We selected 12 best-distributed stations in azimuth with respect to the epicenter (ADK, COR, CPUP, DBIC, ESK, FFC, HRV, KONO, LPAZ, RAR, SJG, SNZO) for the analysis. For the joint inversion we incorporated the 12 broadband teleseismic displacements of the P wave arrival on the vertical component, which were band-pass filtered from 0.01 to 2 Hz, and corrected for the instrumental response before the inversion. Beside the mentioned stations, some other stations in the southern hemisphere also recorded this event; however, since the signal-to-noise ratio for these stations was very poor, we excluded them from the analysis.

For the joint inversion, we used a rupture velocity of 2.8 km/s, and the same fault plane discretization as in the previous case. We computed the synthetic seismograms using the same crustal model shown in Table 2 for the source region, and a general model in Table 3 for the receiver sites. In order to obtain the best agreement between the observed and synthetic time histories, we searched for the optimum weight to assign to each type of data in the inversion; that is, one value for the local and regional data, and another value for teleseismic data. We tested the inversion results for three weighting schemes: 1: 2, 1: 4, 1: 8 (teleseismic: local data) with a normalized error in the misfit between the observed and synthetic seismograms. From this test, we found that the best case was 1:4, with a normalized error of 8.99×10^{-2}. The observed and synthetic seismograms from this final inversion are compared in Figure 8, and the dislocation pattern obtained is shown in Figure 9.

The seismic moment release obtained first by local inversion ($Mo=4.6 \times 10^{26}$ dyn-cm) and second by the joint inversion ($Mo=4.9 \times 10^{26}$ dyn-cm) is very close to those reported by other authors. These values give a mean moment magnitude of Mw=7.1.

COULOMB FAILURE STRESS CHANGE

Mikumo *et al*. (2000) calculated the dynamic stress change inside the fault area of this earthquake, based on the slip distribution obtained from the local seismograms. They found that high stress drop zones are confined to the deeper part of the fault, surrounded by zones with low stress drop. Mikumo *et al*. (1999) also found that the 1997 earthquake took place in the zone of maximum coseismic stress increase due to the 1985 event, and that the 1997 normal faulting earthquake occurred under possible stress transfer from the 1985 earthquake to the interior of the subducting Cocos plate.

In this section, we investigate the possible influence of the 11/01/97 mainshock event on its aftershock seismicity. Taking into account our final distribution of slips, we calculated the coseismic change of the Coulomb failure stress function (ΔCFS) due to this earthquake, not only over the fault plane but also over a vertical cross section perpendicular to the strike direction. To do this, we computed the Coulomb failure stress by the use of the relation $\Delta CFS = \Delta\tau + \mu' \Delta\sigma_n$ (e.g. Harris, 1998), where $\Delta\tau$ is the shear stress change in the direction of the fault slip, $\Delta\sigma_n$ is the change in the tensional stress normal to the fault plane, and μ' is an apparent coefficient of friction $\mu' = \mu(1-p)$, where μ is the static coefficient of friction and p is the pore pressure in the source volume. Here, we used the formulation given by Okada (1985, 1992) to compute the coseismic ΔCFS. In the computations, we used the mean shear modulus for the site, $\mu = 3.5 \times 10^{11}$ dyn/cm^2, with a Poisson ratio of $\nu = 0.25$. For the tectonic apparent coefficient of friction, we used the value of $\mu' = 0.4$ adopted by Mikumo *et al*. (2000) for the Mexican subduction zone.

Figures 10 and 11 shows the ΔCFS plots for this earthquake. In Figure 10, we show the Coulomb failure stress over the fault plane. Here, the "x" axis (abscissa) represents the distance along the strike direction, which is approximately parallel to the coast, and the "y" axis (ordinate) represents the distance in the dip direction also indicating the depth. Contours are given in bars. Black dots show the aftershock hypocenters projected over the fault plane. It can be observed in this figure that most of the aftershocks are distributed over the main asperity inside the zone of stress drop caused by normal faulting. The stress drop zone can be expected to, in turn, become a zone of stress increase for subsequent inverse faulting. Actually, almost all of these aftershocks indicate inverse faulting mechanism (Table 4). The ΔCFS due to the mainshock slips was resolved onto the plane strike=290°, dip=70°, over the cross section A-A' in Figure 11, perpendicular to the main fault plane (see Figure 1). In this figure, we show the plot of ΔCFS contours and the aftershock hypocenters projected over this section. Here we see that almost all of these aftershocks fall inside the contours of stress increase for inverse faulting due to the mainshock, as expected. It is important to note that in this case aftershocks are occurring outside of the fault plane on the downdip side of the slab, which suggests that they are not defining the fault plane.

CONCLUSIONS

The focal mechanism of this event shows a very steep, dip slip normal faulting in the oceanic subducting slab. Although high-angle, inslab normal faulting events are common in the Mexican subduction zone (e.g. Singh *et al*., 1981, 2000), this is the first reported event of a great magnitude with a nearly-vertical mechanism. The falling block in the focal mechanism suggests that the driving mechanism of this event could be related with the gravitational pull of the subducting slab.

On the other hand, the dislocation pattern obtained from the 2D kinematic inversion shows a complex slip distribu-

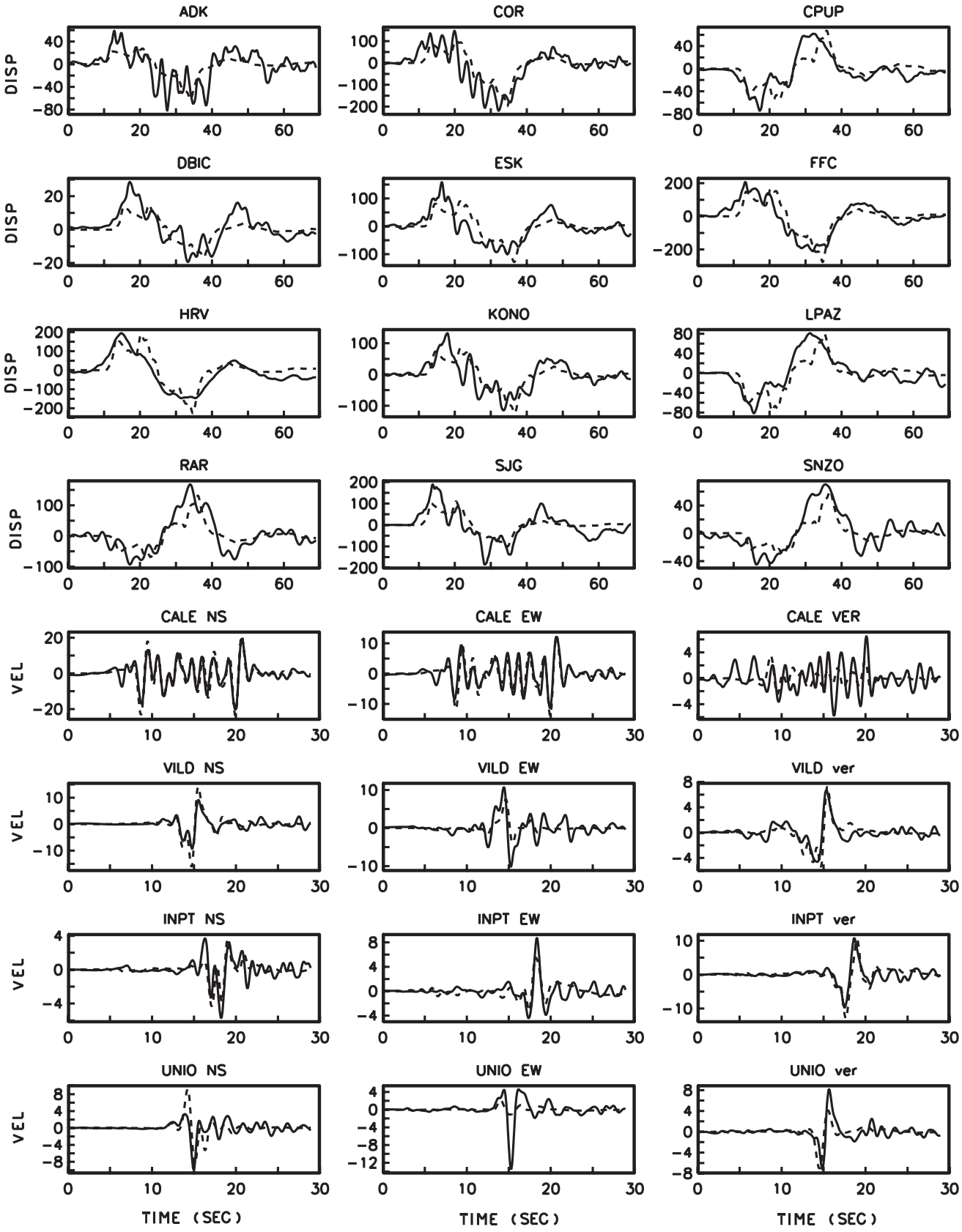

Fig. 8. Comparison between the recorded seismograms (solid lines) and the synthetic seismograms (dashed lines), obtained from the joint linear inversion using displacement teleseimic and velocity local data.

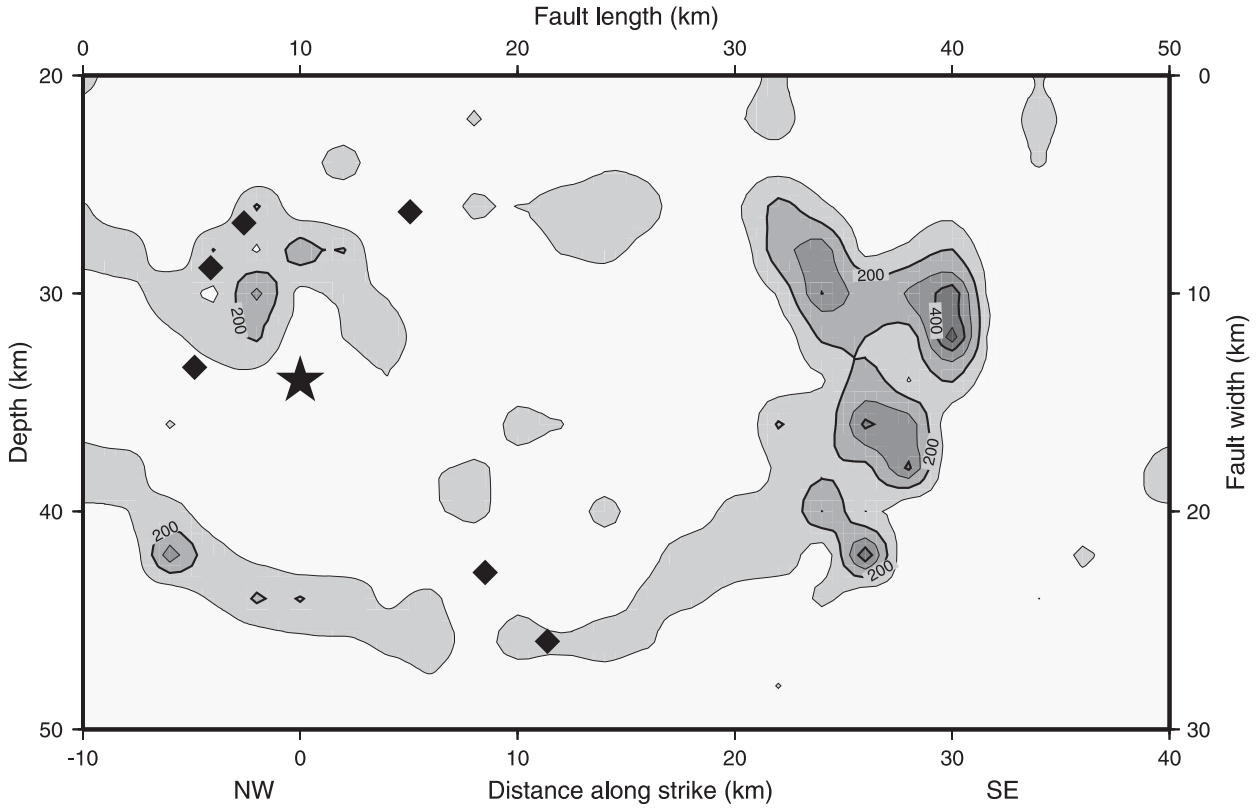

Fig. 9. Dislocation pattern for the 11/01/97 mainshock obtained from the joint linear inversion using both teleseimic and local data. Slips are shown in cm. The thin line outside the gray contours represents a 50 cm curve.

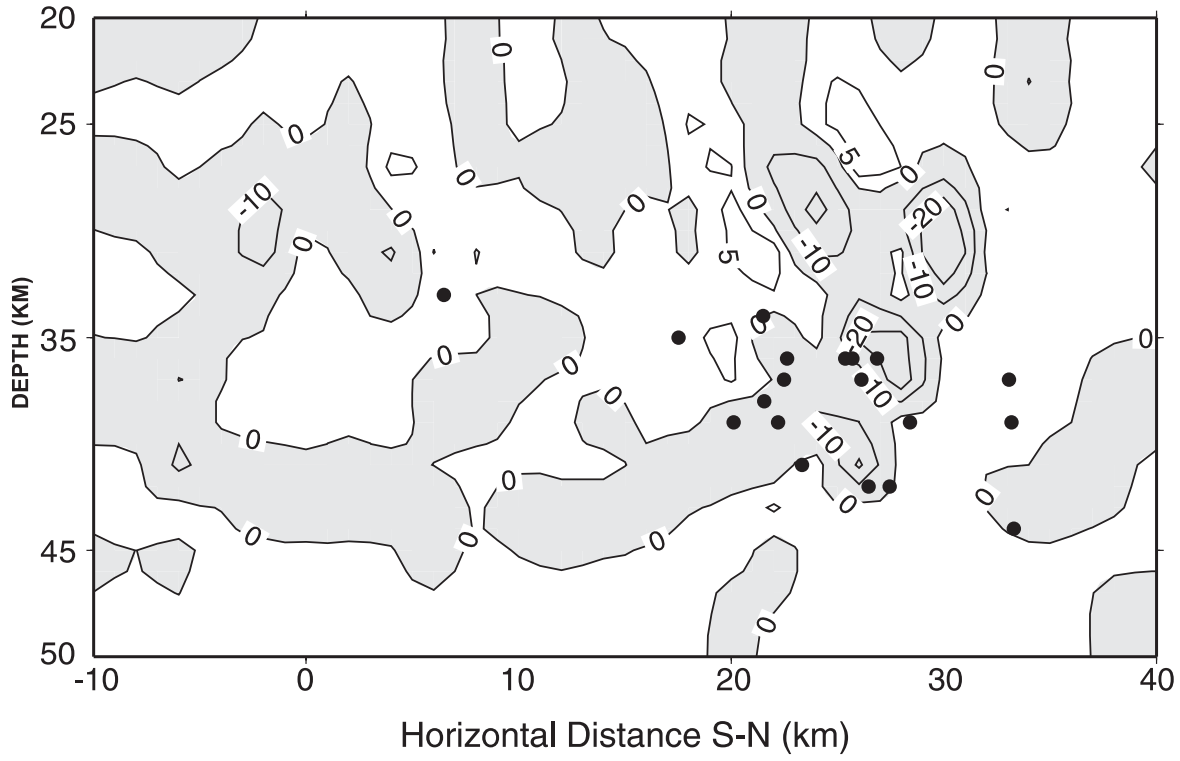

Fig. 10. Coulomb failure stress over the fault plane. Contours are in bars. Black dots indicate the projected aftershock locations over the fault plane.

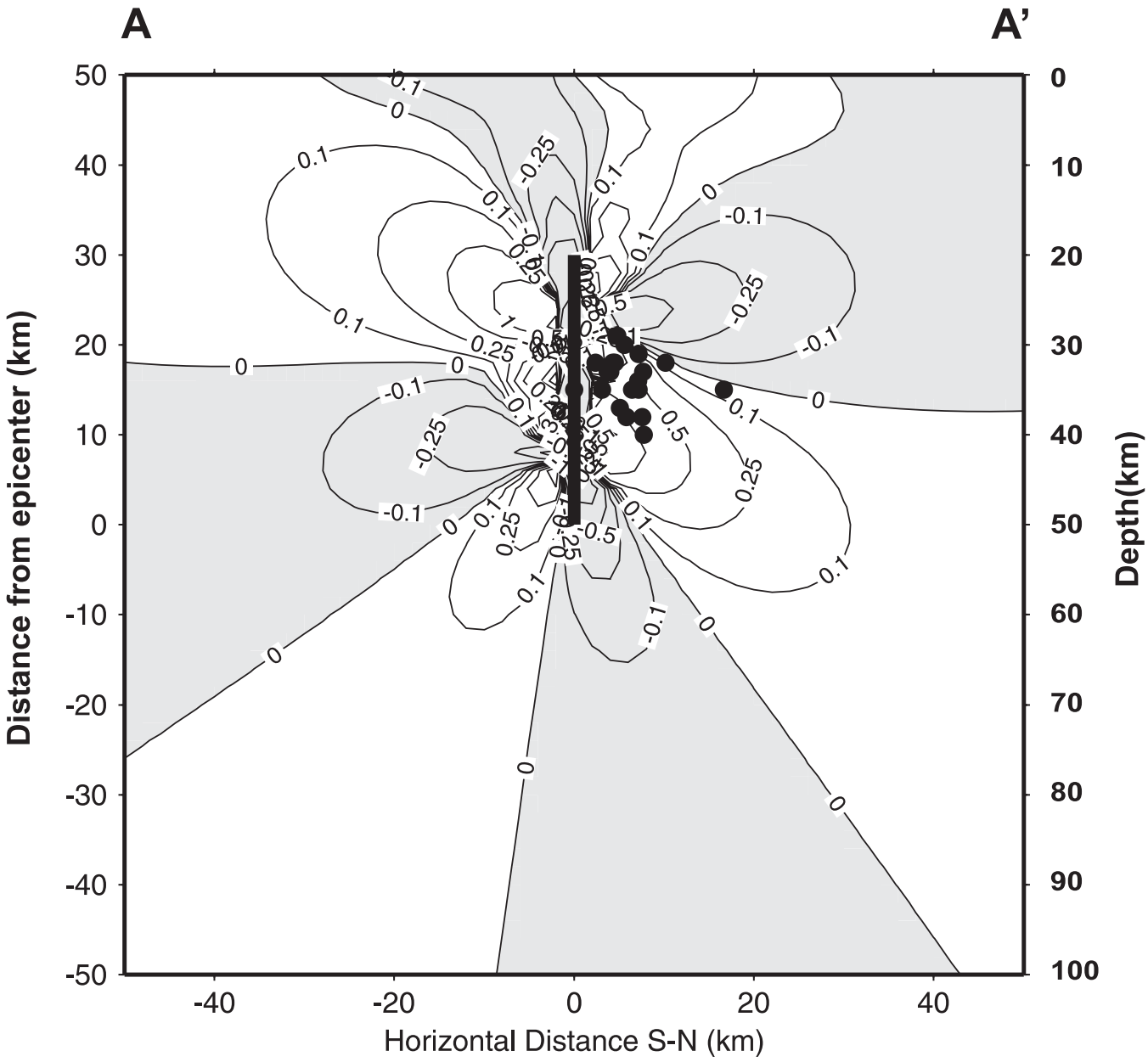

Fig. 11. Cross-section A-A' of Figure 1. Coulomb failure stress is resolved in the direction of the aftershocks focal mechanism. Contours are in bars. Black dots represent the location of the aftershocks projected on plane of the cross-section.

tion, with the main seismic moment release occurring at the southeast of the hypocenter, and breaking a main asperity with an area of approximately 20x30 km (Figure 9). Comparing the slip distribution with the location of its aftershocks, we observe that these aftershocks occurred mainly in the zones of high slip - stress drop on the fault. It is to be noted from the location of their hypocenters that, all the aftershock seismicity seems to have occurred also within the subducted slab. The Coulomb failure stress resolved in the direction of the focal mechanism of the aftershocks (steep-angle, reverse faulting) shows that almost all the aftershock also occurred in the zone of stress increase due to the mainshock, outside of the fault plane, which means that they are not defining the fault plane itself. Several authors have reported a positive correlation between the coseismic stress changes on the neighborhood of the source region, and the increase of seismicity in the stress incresase areas (e.g. King *et al*., 1994; Stein *et al*., 1994; Toda *et al*., 1998; Deng and Sykes, 1997; Harris, 1998; Freed and Lin, 1998; Stein 1999). The results of this study suggest that this aftershock seismicity observed after the occurrence of the 11/01/97 event may have been triggered by the main event.

AKNOWLEDGMENTS

We wish to thank Javier Pacheco for his constructive discussions and remarks. We thank also Roberto Quaas from CENAPRED, Citlalli Pérez from I.I. UNAM and Clara Javier from CFE, for providing the strong motion recordings. Carlos Mendoza kindly provided some codes for the inversion procedures. Synthetics for local distances were computed using the program AXITRA by Olivier Coutant. Synthetics for teleseismic distances were computed based on the program TELEDB by Charles A. Langston.

BIBLIOGRAPHY

BOUCHON, M., 1979. Discrete wave number representation of elastic wave field in three space dimensions. *J. Geophys. Res., 84*, 3609-3614.

BOUCHON, M. and K. AKI, 1977. Discrete wave number representation of seismic source wave fields. *Bull. Seism. Soc. Amer. 67*, 259-277.

DELOUIS, B. and D. LEGRAND, 1999. Focal mechanism determination and identification of the fault plane of earthquakes using only one or two near source seismic recordings. *Bull. Seism. Soc. Amer., 89,* 1558-1574.

DENG, J. and L.R. SYKES, 1997. Evolution of the stress field in southern California and triggering of moderate-size earthquakes: A 200-year perspective *J. Geophys. Res. 102,* 9859-9886.

FREED, A. M. and J. LIN, 1998. Time- dependent changes in failure stress following thrust earthquakes. *J. Geophys. Res.,* 24300-24300.

FUENTES, C., 1997. Determinación de la estructura cortical para el sur de México utilizando dispersión de ondas superficiales. MS dissertation, UNAM, México.

FUTTERMAN, W. I., 1962. Dispersive body waves. *J. Geophys. Res. 67*, 5279-5291.

HARTZELL, S. H. and T. H. HEATON, 1983. Inversion of strong ground motion and teleseismic waveform data, for the fault rupture history of the 1979 Imperial Valley, California, earthquake. *Bull. Seism. Soc. Am., 76*, 1553-1583.

HARRIS, R., 1998. Introduction to special section: stress triggers, stress shadows, and implications for seismic hazards. *J. Geophys. Res. 103,* 24347-24358.

HELMBERGER, D., 1974. Generalized ray theory for shear dislocations. *Bull. Seism. Soc. Am., 64*, 45-64.

IWAN, W. D., M. A. MOSER and C. PENG, 1985. Some observations of strong-motion earthquake measurement using a digital accelerograph. *Bull. Seism. Soc. Amer., 75,* 1225-1246.

KING, G. C. P., R. S. STEIN and J. LIN, 1994. Static stress changes and the triggering of earthquakes. *Bull. Seism. Soc. Am. 84,* 935-953.

LANGSTON, C. and D. HELMBERGER, 1975. A procedure for modelling shallow dislocation sources. *Geophys. J. Roy. Astr. Soc., 42,* 117-130.

LAWSON, C. L. and R. J. HANSON, 1974. Solving least squares problems. Ed. Prentice Hall Inc., Englewood Cliffs, New Jersey, 340p.

MENKE, W., 1989. Geophysical data analysis: Discrete inverse theory. Ed. Academic Press Inc., San Diego, CA., USA, 289p.

MIKUMO, T., S. K. SINGH and M. A. SANTOYO, 1999. A possible stress interaction between large thrust and normalfaulting earthquakes in the mexican subduction zone. *Bull. Seism. Soc. Am., 89, 6,* 1418-1427.

MIKUMO, T., M. A. SANTOYO and S. K. SINGH, 2000. Dynamic rupture and stress change in normal faulting earthquakes in subducting Cocos plate. *Geophys. J. Int., 140*, 611-620.

NABELEK, J. L., 1984. Determination of earthquake source parameters from inversion of body waves. PhD. dissertation, Massachusetts Institute of Technology, Cambridge, Mass.

OKADA, Y., 1985. Surface deformation due to shear and tensile faults in a half space. *Bull. Seism. Soc. Am. 75,* 1135-1154.

OKADA, Y., 1992. Internal deformation due to shear and tensile faults in a half space. *Bull. Seism. Soc. Am. 82*, 1018-1040.

SINGH, S. K., J. HAVSKOV and L. ASTIZ, 1981. Seismic gaps and recurrence periods of large earthquakes along the Mexican subduction zone. *Bull. Seim. Soc. Am., 71,* 827-843.

SINGH, S. K., M. ORDAZ, L. ALCÁNTARA, N. SHAPIRO, V. KOSTOGLODOV, J. PACHECO, S. ALCOCER, C. GUTIÉRREZ, R. QUAAS, T. MIKUMO and E. OVANDO, 2000. The Oaxaca earthquake of September

30, 1999 (Mw=7.5): A normal faulting event in the subducted Cocos plate. *Seism. Res. Lett., 71,* 67-78.

STEIN, S., 1999. The role of stress transfer in earthquake occurrence. *Nature, 402,* 605-609.

STEIN, R. S., G. C. P. KING and J. LIN, 1994. Stress triggering of the 1994 M=6.7 Northridge, California earthquake by its predecesors. *Science, 265,* 1432-1435.

TODA, S., R. S. STEIN, P. A. REASENBERG, J. H. DIETERICH and A. YOSHIDA, 1998. Stress transferred by the 1995 Mw=6.9 Kobe, Japan, shock: Effect on aftershocks and future earthquake probabilities. *J. Geophys. Res. 103*, 24543-24565.

UNAM SEISMOLOGY GROUP, 1986. The September 1985 Michoacán earthquakes: Aftershock distribution and history of rupture. *Geophys. Res. Lett. 13,* 573-576.

Miguel A. Santoyo, Shri K. Singh and
Takeshi Mikumo

Instituto de Geofísica, UNAM, Ciudad Universitaria,
04510 México D.F., México
Email: masantoyo@correo.unam.mx